Deep Learning–based Reconstruction for Lower-Dose Pediatric CT: Technical Principles, Image Characteristics, and Clinical Implementations

Yasunori Nagayama, MD, PhD
Daisuke Sakabe, PhD
Makoto Goto, RT
Takafumi Emoto, RT
Seitaro Oda, MD, PhD
Takeshi Nakaura, MD, PhD
Masafumi Kidoh, MD, PhD
Hiroyuki Uetani, MD, PhD
Yoshinori Funama, PhD
Toshinori Hirai, MD, PhD

Abbreviations: CNN = convolutional neural network, $CTDI_{vol}$ = volume CT dose index, DLR = deep learning–based reconstruction, FBP = filtered back projection, HIR = hybrid IR, IR = iterative reconstruction, MBIR = model-based IR

RadioGraphics 2021; 41:1936–1953

https://doi.org/10.1148/rg.2021210105

Content Codes: CT IN PD PH

From the Department of Diagnostic Radiology, Graduate School of Medical Sciences (Y.N., S.O., T.N., M.K., H.U., T.H.), and Department of Medical Radiation Sciences, Faculty of Life Sciences (Y.F.), Kumamoto University, 1-1-1 Honjo, Chuo-ku, Kumamoto 860-8556, Japan; and Department of Central Radiology, Kumamoto University Hospital, Chuo-ku, Kumamoto, Japan (D.S., M.G., T.E.). Presented as an education exhibit at the 2020 RSNA Annual Meeting. Received April 4, 2021; revision requested May 14 and received June 10; accepted June 17. For this journal-based SA-CME activity, the author T.H. has provided disclosures (see end of article); all other authors, the editor, and the reviewers have disclosed no relevant relationships. **Address correspondence to** Y.N. (e-mail: *y.nagayama1980@gmail.com*).

Supported by KAKENHI grant 19K17173 from the Japan Society for the Promotion of Science.

SA-CME LEARNING OBJECTIVES

After completing this journal-based SA-CME activity, participants will be able to:

- Understand the basic concepts and technical principles of DLR.
- Describe the image characteristics of DLR and compare them with those of FBP and IR, particularly in lower-dose settings.
- Recognize the effect of DLR on image quality in low-dose pediatric CT for various diagnostic tasks.

See rsna.org/learning-center-rg.

Optimizing the CT acquisition parameters to obtain diagnostic image quality at the lowest possible radiation dose is crucial in the radiosensitive pediatric population. The image quality of low-dose CT can be severely degraded by increased image noise with filtered back projection (FBP) reconstruction. Iterative reconstruction (IR) techniques partially resolve the trade-off relationship between noise and radiation dose but still suffer from degraded noise texture and low-contrast detectability at considerably low-dose settings. Furthermore, sophisticated model-based IR usually requires a long reconstruction time, which restricts its clinical usability. With recent advances in artificial intelligence technology, deep learning–based reconstruction (DLR) has been introduced to overcome the limitations of the FBP and IR approaches and is currently available clinically. DLR incorporates convolutional neural networks—which comprise multiple layers of mathematical equations—into the image reconstruction process to reduce image noise, improve spatial resolution, and preserve preferable noise texture in the CT images. For DLR development, numerous network parameters are iteratively optimized through an extensive learning process to discriminate true attenuation from noise by using low-dose training and high-dose teaching image data. After rigorous validations of network generalizability, the DLR engine can be used to generate high-quality images from low-dose projection data in a short reconstruction time in a clinical environment. Application of the DLR technique allows substantial dose reduction in pediatric CT performed for various clinical indications while preserving the diagnostic image quality. The authors present an overview of the basic concept, technical principles, and image characteristics of DLR and its clinical feasibility for low-dose pediatric CT.

Introduction

In the past few decades, use of CT has increased dramatically owing to its excellent diagnostic performance, easy accessibility, short scanning time, and cost-effectiveness (1,2). Although the widespread use of CT has led to tremendous advances in modern medical practice, concerns regarding the possible adverse effects associated with increased radiation exposure from CT scans have concomitantly increased, particularly in pediatric populations, as they are sensitive to the possible stochastic effects of ionizing radiation and have many remaining years for the cancer to develop (1,2). Although the true risks of low-dose radiation (<100 mSv) remain unclear and the clinical benefits of appropriate CT use are certain, some epidemiologic surveys (3–6) and biologic studies

TEACHING POINTS

- Owing to simplified approximations in the data acquisition process, FBP cannot account for measurement errors from unideal properties such as Poisson statistical variations, scatter, or beam-hardening effect, leading to amplified noise and artifacts in low-dose CT.
- The noise texture of IR images often differs from that of the traditional FBP images, which can negatively affect subjective acceptance and diagnostic confidence. The image appearance is expressed as "plasticlike," "oil painting," "blotchy," "pixelated," or "blurring," which becomes more prominent when high-strength levels of HIR or MBIR are applied for projection data acquired with substantially reduced dose settings.
- Although IR allows drastic dose reduction for high-contrast diagnostic tasks, such as detection of solid lung nodules and urinary stones, preservation of low-contrast object detectability can be challenging even if the noise magnitude (ie, fluctuations of pixel values in a homogeneous region of interest) is reduced by IR algorithms.
- For development of the DLR engine, a CNN is trained to extract statistical features that differentiate noise from true attenuation by using high-quality images acquired under the ideal conditions as target data and low-quality images as training data.
- IR techniques yield reduction of the high-frequency noise component but have limited performance for reducing the low-frequency noise component, leading to a unique unnatural image appearance, particularly at low-dose settings. DLR effectively suppresses low-spatial-frequency noise, yielding natural and preferable noise texture.

(7,8) have highlighted the possible carcinogenic effects and the dose-response relationships in pediatric CT. Therefore, promoting rigorous adherence to the "as low as reasonably achievable" (ALARA) principle is crucial to minimize the possible risks of ionizing radiation exposure from pediatric CT.

Appropriate justifications and consideration of alternative diagnostic imaging modalities, such as US and MRI, for each clinical condition are the most important steps to avoid unnecessary ionizing radiation exposure from CT (9). Application of various dose-optimization techniques, such as automated tube current modulation, lowering tube voltage, high-pitch acquisition, and x-ray spectral shaping, in conjunction with following the guidelines for appropriate CT use, can substantially reduce the overall radiation dose (10–13). However, lowering the radiation dose amplifies the noise in CT images owing to decreased photon penetration—regardless of the scanning technique used—potentially degrading the diagnostic value of examinations. Improving spatial resolution and reducing section thickness are usually required for detailed assessment of children's small anatomic structures, which can lead to a further increase in noise and degradation of low-contrast spatial resolution (14). Therefore, implementation of image processing techniques that minimize image noise and preserve adequate spatial and contrast resolution is a key factor for successful low-dose pediatric CT.

Recently, deep learning–based reconstruction (DLR) techniques that incorporate convolutional neural networks (CNNs) into the CT reconstruction process to remove image noise and improve spatial resolution have become clinically available. Use of this novel reconstruction approach is expected to facilitate substantial dose reduction in pediatric CT while maintaining the diagnostic image quality. This article provides an overview of the basic concept and technical principles of DLR and the characteristics of DLR images and demonstrates the clinical feasibility and dose reduction capability of DLR for pediatric CT in various clinical indications.

Current Standard CT Reconstruction Techniques

CT scanners acquire x-ray projection data by transmitting a fan of photons emitted from an x-ray source through the body to a detector array. CT image reconstruction is a mathematical process in which the projection data from multiple angles are transformed into tomographic images by assigning attenuation values to each voxel (15–18). Reconstruction techniques considerably affect the image quality and the radiation doses required to obtain adequate anatomic and pathologic information for a given clinical task. Currently, filtered back projection (FBP) and iterative reconstruction (IR) are widely used clinically for CT reconstruction. In this section, the advantages and disadvantages of these reconstruction techniques are discussed to highlight the reasons for developing the DLR techniques.

Filtered Back Projection

FBP is an analytic approach that has long been the standard reference technique in CT image reconstruction because of its numerical robustness, short processing time, and computational efficiency. For FBP reconstruction, measured projections (ie, sinogram data) are first processed with a convolutional filter to compensate for low-pass blurring caused by the nonuniform data sampling inherent to the CT acquisition process. Next, the filtered projection data are transformed into the image space via back projection to generate the final FBP images (Fig 1A) (16–18).

Different-strength filters or kernels can be selected to optimize the image quality according to clinical tasks and anatomic regions of interest. "Sharp" kernels can be used in evaluating fine high-contrast objects such as lung and bone, whereas "soft" kernels are usually applied for

diagnostic tasks involving low-contrast object detection, such as brain and hepatic CT.

The FBP method relies on multiple unrealistic assumptions, such as a point x-ray source, a pencil x-ray beam geometry, a central point of detector elements, and noise-free projection data. Owing to simplified approximations in the data acquisition process, FBP cannot account for measurement errors from unideal properties such as Poisson statistical variations, scatter, or beam-hardening effect, leading to amplified noise and artifacts in low-dose CT.

In FBP images, the image noise increases approximately inversely proportional to the square root of the tube current and section thickness (19). Use of soft kernels or thick sections can compensate for increased noise but obscures the fine details and edge information because of the inherent trade-off between spatial resolution and noise magnitude (16,17).

Iterative Reconstruction

IR is a reconstruction technique that iteratively minimizes an objective function to satisfy predefined convergence criteria in calculating image data. Although the IR approach was proposed in the early 1970s, it has not been available until recently owing to its mathematically demanding property. Owing to improved computational power, various IR algorithms have been clinically introduced since 2009 with the goal of reducing image noise and enabling low-dose CT without loss of diagnostic image quality (16–18). IR algorithms are classified roughly into two classes: hybrid IR (HIR or statistical IR) and model-based IR (MBIR), with slight differences in technical details between manufacturers.

The HIR technique—which combines analytic and iterative approaches—is characterized by separate iterative data filtering in the projection space and/or image space to reduce the noise and artifacts (Fig 1B). In the projection space, severely noise-contaminated or photon-starved projections are identified on the basis of photon and noise statistical modeling. A lower weight is assigned for high-noise projections than for low-noise projections to reduce the noise contribution of the projections.

The modified projections are back projected into the image space, where the data are iteratively filtered using statistical and anatomic models to minimize the magnitude of quantum noise, enabling further removal of image noise. Of note, only a single back projection is carried out in HIR; thus, the reconstruction speed of HIR is almost equivalent to that of FBP. Nevertheless, its performance for reducing noise and artifacts without loss of spatial resolution is relatively limited because it relies on simplified assumptions for system and physics models, as in the analytic FBP approach (17,19).

The MBIR technique is characterized by repetitive backward and forward projection processes for iterative improvement of the reconstructed image data (Fig 1C). The artificial projection is generated from the initial image estimation derived from the original sinogram through forward projection and compared with the measured projection. Next, the artificial data are corrected to reduce the deviation from the measured projections. The corrected data are back projected to generate the updated image data. The same cyclic process is repeated until the difference between the measured and artificial projections meets convergence criteria.

The forward projection step requires accurate models for the system and physical factors involved in the data acquisition process, such as the shape of the detector, focal spot, x-ray beam spectrum, and scattering. Therefore, the MBIR approach is far more computationally demanding compared with FBP and HIR, although complex phenomena may still be simplified and approximated on the basis of theoretical understanding and prior knowledge of physics, statistics, image properties, and engineering to make models mathematically manageable (17). The capabilities of MBIR for noise and artifact reduction and spatial resolution improvement are usually superior to those of HIR (17,19).

Limitations of IR Approach in Low-Dose CT

Despite substantial contributions to CT dose optimization, the IR approach still has several limitations. The noise texture of IR images often differs from that of the traditional FBP images, which can negatively affect subjective acceptance and diagnostic confidence. The image appearance is expressed as "plasticlike," "oil painting," "blotchy," "pixelated," or "blurring," which becomes more prominent when high-strength levels of HIR or MBIR are applied for projection data acquired with substantially reduced dose settings (16,17,20). The alteration of noise texture may be related to IR's limited performance for reducing low-spatial-frequency noise components and preserving low-contrast spatial resolution. In contrast to FBP images, IR images show nonlinear spatial resolution as a function of dose level and object contrast (21–23).

In addition, the relationship between the radiation dose and noise magnitude seen in FBP images is no longer applicable to IR images (23,24). Although IR allows drastic dose reduction for high-contrast diagnostic tasks, such as detection

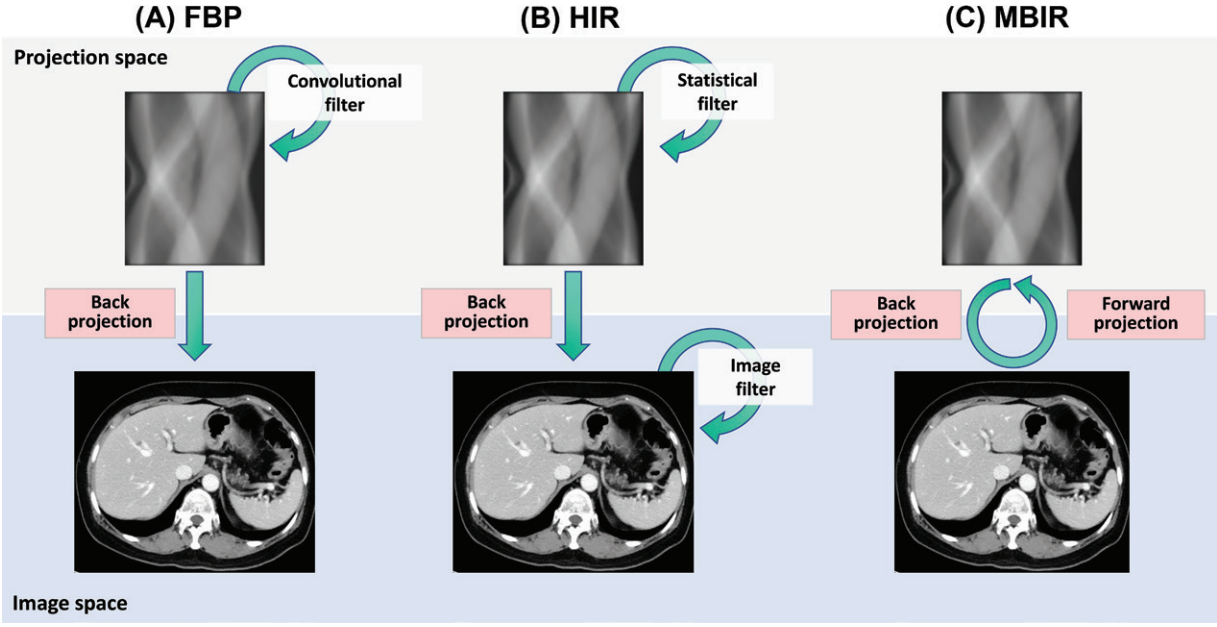

Figure 1. CT reconstruction techniques. **(A)** In FBP, a linear-mathematical operation with a convolutional filter (kernel) is initially applied to sinogram data to remove low-pass blurring and preserve spatial resolution. Then, filtered data are back projected into the image space to obtain the final images. **(B)** In hybrid IR (HIR), sinogram data are iteratively filtered in the projection and/or image space to reduce artifacts and noise. **(C)** In model-based IR (MBIR), the sinogram data are back projected to create an initial image estimation. Then, artificial projection data are synthesized through forward projection and compared with the measured projection to update the initial image estimation. This process is repeated until the difference between the measured and artificial projections is minimized or predefined criteria are satisfied.

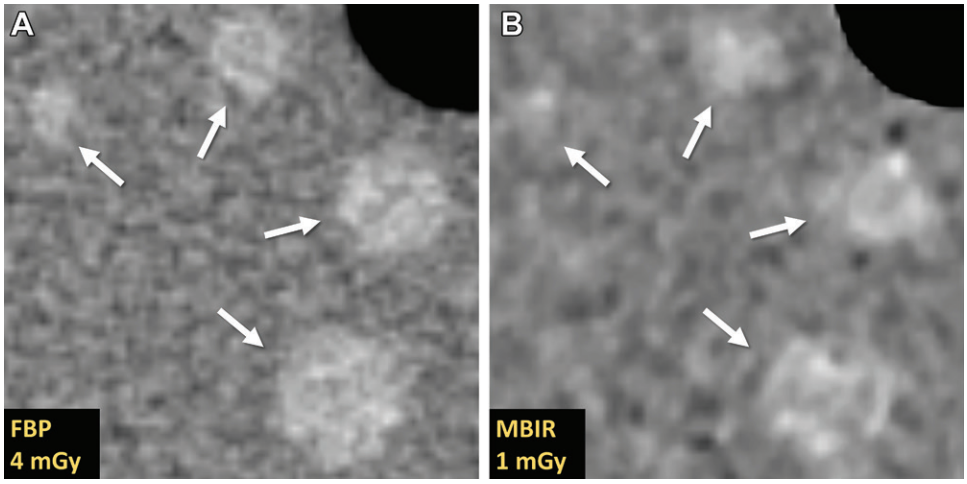

Figure 2. Comparisons of noise magnitude, noise texture, and delineation of low-contrast objects between FBP **(A)** and MBIR **(B)** images. The FBP image was acquired with a volume CT dose index ($CTDI_{vol}$) of 4 mGy, and the MBIR image was obtained with a $CTDI_{vol}$ of 1 mGy. Noise magnitude measured as the standard deviation of CT attenuation is equivalent in both images (18 HU), whereas noise texture and depiction of low-contrast objects are considerably degraded in lower-dose MBIR.

of solid lung nodules and urinary stones, preservation of low-contrast object detectability can be challenging even if the noise magnitude (ie, fluctuations of pixel values in a homogeneous region of interest) is reduced by IR algorithms (Fig 2) (25,26). These limitations may reflect that IR can handle a relatively small number of parameters for modeling complex acquisition processes, and simplified modeling can lead to unreliable overcorrection in the final images at low-dose settings.

Furthermore, MBIR requires a longer reconstruction time (ranging from several minutes to hours depending on scan length, section thickness, and algorithms used) than FBP and HIR, which usually require less than 1 minute and allow almost real-time image reconstruction. This can hamper workflow in the busy clinical practice. Therefore, a novel CT reconstruction approach that can overcome the drawbacks of IR techniques is warranted.

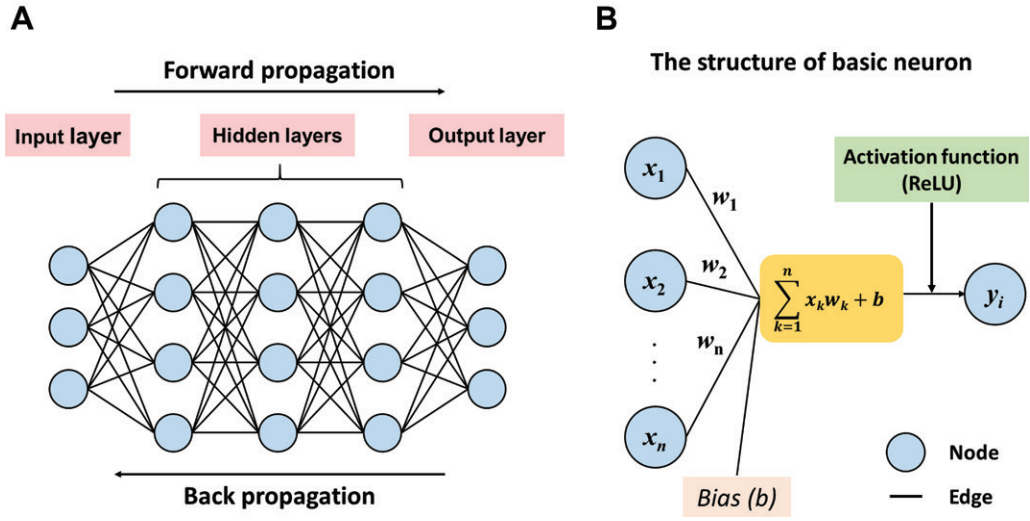

Figure 3. Typical architecture of a deep artificial neural network. **(A)** Deep learning usually utilizes artificial neural networks, including multiple hidden layers between input and output layers. The input layer receives input data, the hidden layers extract the features of input data, and the output layer produces the results of data processing. Each node at each layer is sequentially activated from the input layer to the output layer (forward propagation) to obtain a prediction from the input data. **(B)** Each input is multiplied by its weight (w_i), all the multiplications are summed, and a constant value called bias is added. The result is processed with a nonlinear activation function such as the rectified linear unit *(ReLU)*—defined as [$f(x) = \max(0, x)$]—to output data y_i. The previous layer's output data serve as input data in the next layer unless this is an output layer. To train a neural network, model performance is calculated with a loss function and weights are optimized via optimization algorithms (back propagation).

Overview of Deep Learning and CNNs

Given the remarkable improvements in computational power and the development of sophisticated algorithms over the past few years, artificial intelligence (AI) is rapidly being used in various daily tasks, including the health care field (27). Machine learning is a subclass of AI that can learn and improve its performance on the basis of its experience without preprogrammed explicit rules (27–32). In traditional machine learning, human experts need to choose and encode features that are best suited for solving problems, the process of which is called feature engineering. Next, statistical classifiers—such as support vector machines and random forests—are used to analyze the handcrafted features. However, predefining the optimal features is extremely challenging and time-consuming, particularly in image recognition tasks (27,28).

Deep learning, a class of machine learning, learns and extracts the best features directly from raw data on its own without requiring feature engineering. Typical deep learning utilizes an artificial neural network with multiple hidden layers, where the artificial neurons or nodes are connected with varied learnable weights (Fig 3). The neural network learns to output accurate predictions from the input data by optimizing each node's weight through repeated forward and back propagation processes. A deep learning model including millions of parameters can acquire the ability to deal with extremely complex tasks through the training process, overcoming the challenges of traditional handcrafted modeling solutions.

Among deep-learning models, CNN learns spatial hierarchies of features and has been most commonly used for processing image data. A CNN is typically composed of a convolution layer, pooling layer, and fully connected layer (Fig 4), among which the convolution layer is the fundamental element, while the latter two layers can be eliminated to optimize the learning performance. CNN training is a process of optimizing learnable network parameters (ie, kernels and weights in the convolution and fully connected layers, respectively) to minimize the discrepancies between output estimation and ground truth. The performance of a model under certain network parameters is calculated by a loss function, and the parameters are iteratively updated via mathematical optimization algorithms.

CNN architectures have evolved rapidly in the past few years. In particular, the residual learning framework, which implements shortcut connections that enable the network to learn the residual function instead of the target function itself (33), and the batch-normalization techniques, which transform the mean and variance of input data to 0 and 1, respectively (34), have been shown to boost training efficacy for deeper neural

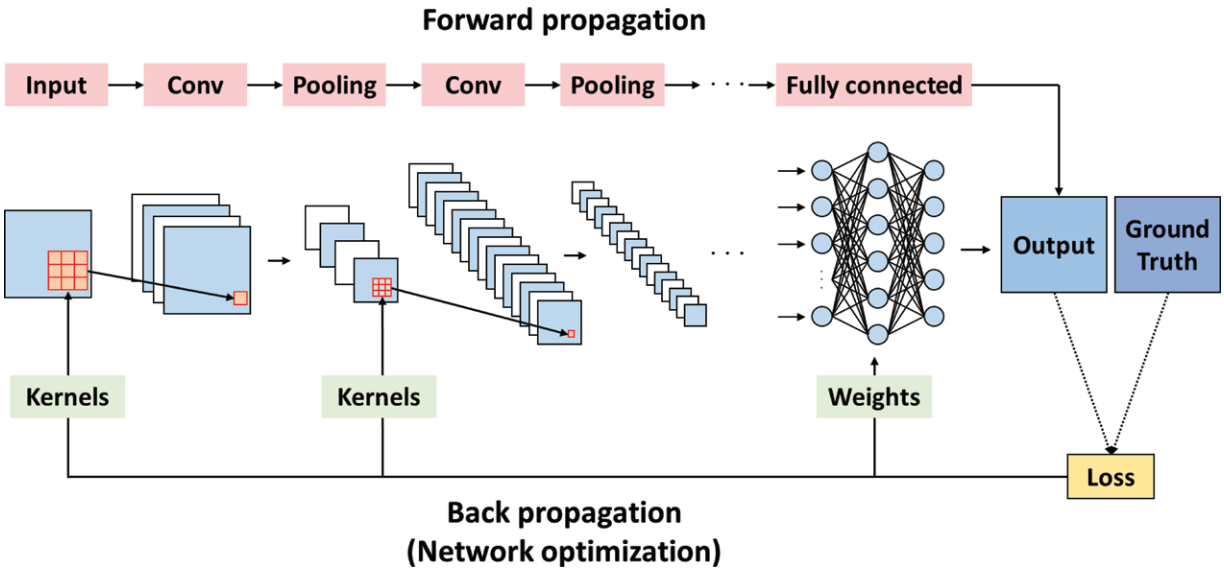

Figure 4. CNN. Input data are firstly processed at convolutional layers *(Conv)*, where learnable mathematical convolution filters called kernels and a nonlinear activation function (most commonly the rectified linear unit [ReLU]) are applied to extract features. The pooling layers reduce the spatial dimensions of feature maps. Fully connected layers serve as classifiers to obtain the final output. Network performance under particular learnable parameters (ie, kernels in convolutional layers and weights in fully connected layers) is calculated with a loss function through forward propagation, and parameters are optimized to reduce loss through back propagation.

networks. A variety of proposed networks have achieved great success in detection, classification, segmentation, and image generation tasks in the field of diagnostic radiology (35–38). Various recent publications have provided further basic knowledge to facilitate understanding of deep learning and CNN technologies (27–32).

Deep Learning–based CT Reconstruction

Basic Concept and Technical Principles

As discussed earlier, reducing CT image noise without compromising noise texture, spatial resolution, and low-contrast object detectability is a complex and challenging task involving numerous factors that the IR approach cannot fully handle. DLR aims to create high-quality images that outperform MBIR in terms of noise texture, dose efficiency, and processing speed by implementing the CNN-based denoising algorithm in the CT reconstruction process. For development of the DLR engine, a CNN is trained to extract statistical features that differentiate noise from true attenuation by using high-quality images acquired under the ideal conditions as target data and low-quality images as training data. Among the various proposed DLRs, CNN architectures incorporating residual learning with batch-normalization techniques have been popularly used to enhance training efficiency and denoising performance (39,40).

The standard CNN model used for DLR creates the output CT images from low-quality image input data through forward propagation in the learning process. The output image's features are compared with those of the ground-truth high-quality images with respect to noise magnitude, noise texture, and spatial resolution. Then, the network parameters are automatically optimized to reduce discrepancies. DLR is required to remove the image noise and preserve the depiction of anatomic and pathologic details without sacrificing the noise texture. The input-forward, error–back propagation process is repeated iteratively until the network is fully optimized and produces output images that exactly match the high-quality target images.

Once the training process is completed, a large number of independent clinical and phantom images, acquired at various dose settings that have never been used in the training process, are reconstructed with the trained network and are extensively tested by radiologists and medical physicians to ensure wide applicability and robustness. After rigorously validating the network generalizability under various realistic conditions, the CNN-based DLR engine can be used to generate high-quality images from low-dose projection data with a considerably higher speed than MBIR in a clinical environment (Fig 5).

Commercially Available DLR Algorithms

Currently, two types of vendor-specific DLR algorithms implemented in CT scanners are available clinically. The first commercialized DLR algorithm is the Advanced Intelligent Clear-IQ Engine (AiCE) (Canon Medical Systems). For

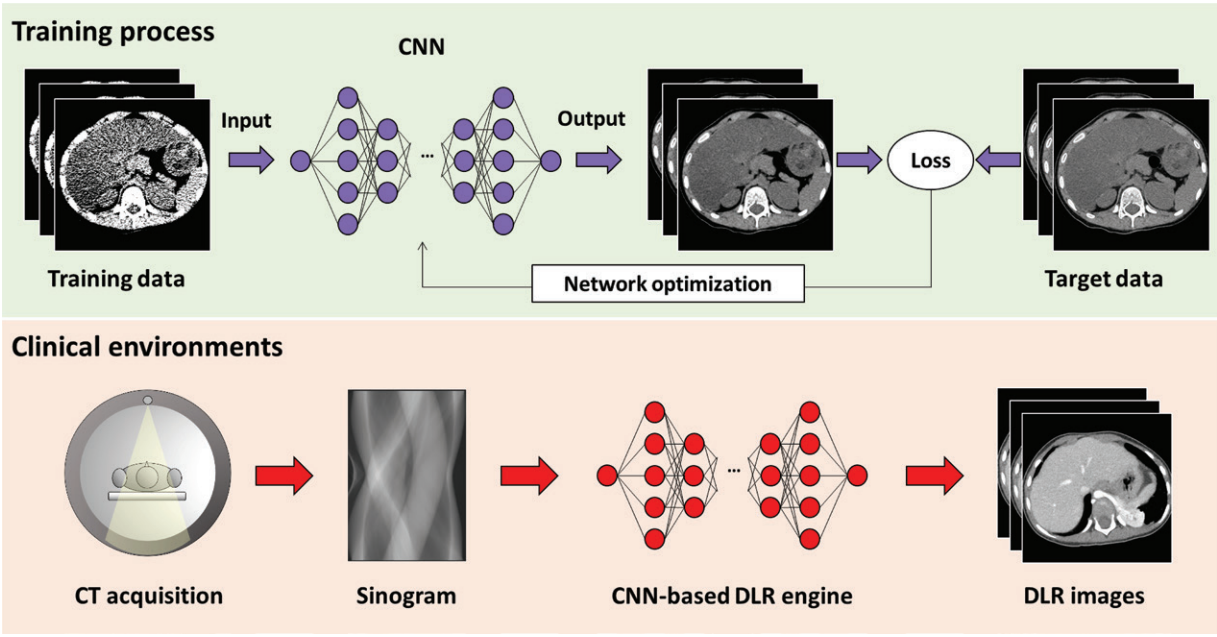

Figure 5. DLR. For development of DLR, a CNN is trained to extract statistical features that differentiate noise from true attenuation using low-quality training and high-quality target image data. The CNN model creates the temporal output CT images from input low-quality image data in the learning process. The features of the temporal output images are compared with those of the target images, and the network parameters are optimized to reduce discrepancies. The input-forward, error–back propagation process is repeated until the network has fully learned to produce output images that exactly match the target images. After completion of network training, a CNN-based DLR engine can be used to obtain high-quality DLR images with fast reconstruction speed in a clinical environment.

development of the AiCE algorithm, simulated low-dose HIR data and high-dose MBIR data are used as training input and training target, respectively. The reconstruction of the target images is subjected to a much larger number of iterations than the commercially available MBIR to achieve the best possible image quality.

In clinical environments, the trained DLR engine is applied to the HIR images to generate high-quality AiCE images (41–43). A variety of reconstruction modes specialized for given anatomic areas and clinical tasks (eg, body, lung, brain, and cardiac) are available. The calculation time of AiCE is reported to be approximately three to five times faster than that of MBIR (41).

Another commercially available DLR algorithm is TrueFidelity (GE Healthcare). This algorithm uses higher-dose FBP images as target data on the basis of the concept of replicating the noise texture and visual impression of the FBP images that are familiar to most radiologists (44). Unlike the AiCE algorithm, the TrueFidelity engine produces the DLR images directly from the projection data. At this time, details of the CNN architecture and training and validation processes have not been fully disclosed. A single soft-tissue mode with three strength levels is available for clinical use.

To date, there have been no available data or reports that directly compare the image characteristics, reconstruction time, diagnostic performance, and possible limitations between different DLR algorithms, which may be an interesting research subject for future studies.

Image Characteristics of DLR

Appropriate image quality assessment is crucial to clarify the diagnostic performance and dose-reduction potential of each reconstruction technique, particularly when mathematically complex nonlinear noise-reduction algorithms are used. In this section, we present the image characteristics of DLR in terms of noise magnitude, noise texture, and depiction of high- and low-contrast objects and compare them with those of FBP, HIR, and MBIR to estimate the possible dose-reduction capabilities of DLR. All DLR images were reconstructed using the AiCE algorithms optimized for soft-tissue assessment ("body-sharp" mode).

Noise Magnitude

The standard deviation of CT attenuation within a region of interest placed in homogeneous structures was used as a first-order metric for the noise magnitude. The phantom experiments revealed that the noise-reduction performance of DLR relative to traditional FBP was superior to that of HIR and MBIR at lower dose ranges. In contrast, MBIR showed the lowest noise at the

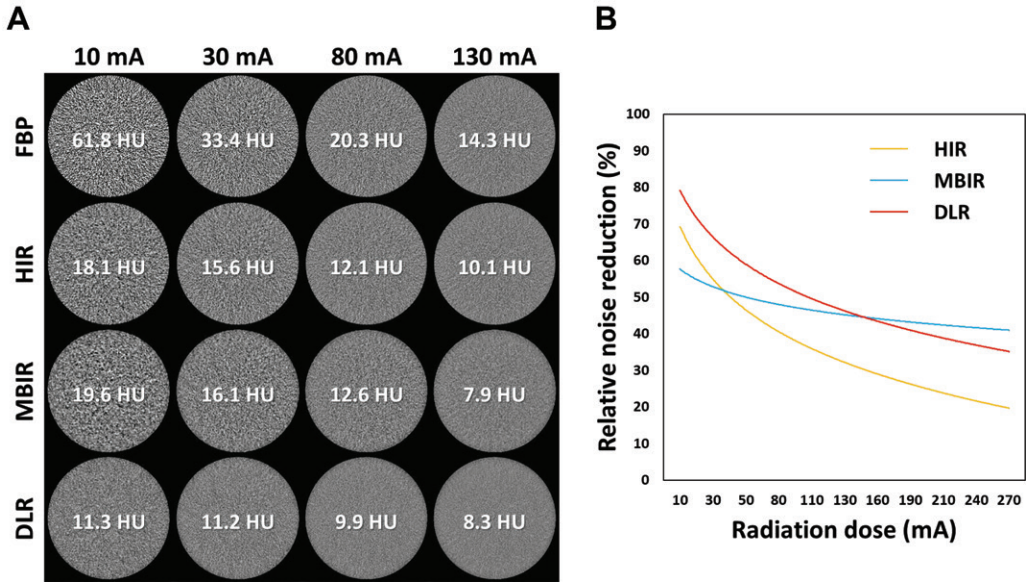

Figure 6. Phantom CT images demonstrating the noise magnitude **(A)** and graph showing the noise-reduction performance **(B)** of HIR, MBIR, and DLR relative to FBP at different dose settings. The reconstruction time for the FBP, HIR, MBIR, and DLR images was 10, 13, 191, and 30 seconds, respectively.

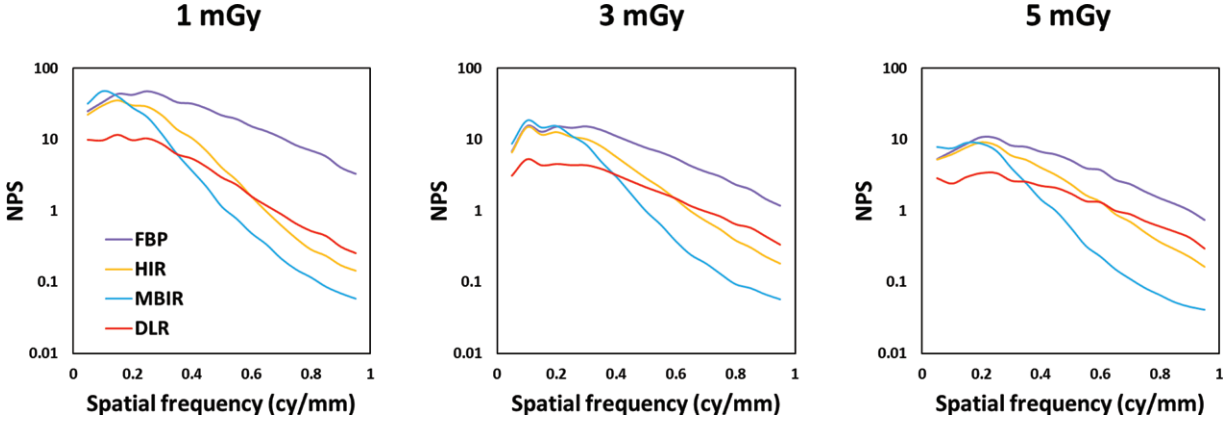

Figure 7. Noise power spectrum *(NPS)* curves at three dose levels obtained with FBP, HIR, MBIR, and DLR. The low-spatial-frequency noise component that leads to coarse and blurred image appearance is most effectively reduced with DLR at all dose levels. *cy* = cycles.

higher dose ranges (45), suggesting that DLR is the most suitable reconstruction technique for obtaining the lowest-noise image in low-dose pediatric CT (Fig 6).

Noise Texture

Image noise can be characterized by not only its magnitude but also its texture. Images with equivalent noise magnitude but different noise texture provide considerably altered visual impressions and object conspicuity. The texture can be quantitatively assessed with a noise power spectrum that measures the amount of noise at each spatial frequency. The noise power concentrated at higher frequencies leads to a finer and sharper image appearance, whereas that at lower frequencies provides a coarser and blurred impression (20), potentially deteriorating the subjective acceptability and low-contrast spatial resolution.

IR techniques yield reduction of the high-frequency noise component but have limited performance for reducing the low-frequency noise component, leading to a unique unnatural image appearance, particularly at low-dose settings (46). DLR effectively suppresses low-spatial-frequency noise (45,47,48) (Fig 7), yielding natural and preferable noise texture.

Depiction of Small High-Contrast Object

In FBP-based images, the ability to depict small high-contrast objects (ie, high-contrast spatial resolution) is generally independent of radiation dose levels when the same kernel is applied (Fig 8a) (20,21,45,49). By comparison, depiction of the same objects is deteriorated in HIR images

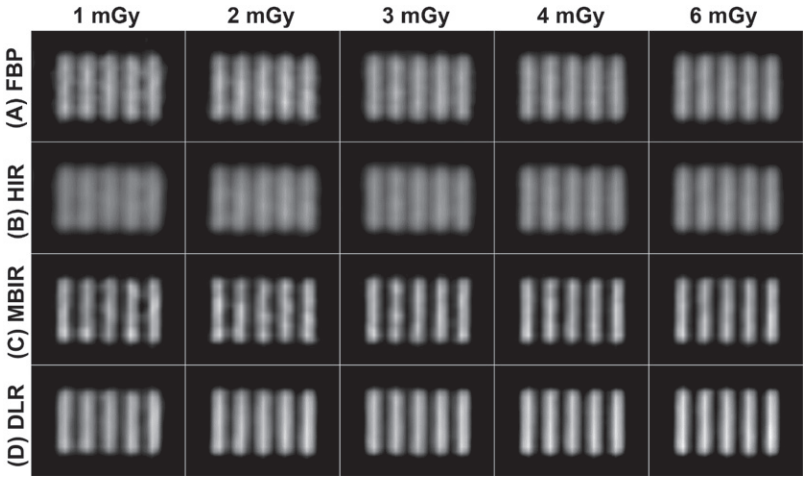

Figure 8. CT images of high-contrast bar pattern (each line = 1 mm in width) obtained at varying dose levels. **(A)** In the FBP images, the resolution is almost independent of the radiation dose level. **(B)** In HIR, the depiction is deteriorated at the lower dose levels. **(C)** MBIR yields the highest spatial resolution, but the line margin becomes irregular at the lower dose levels. **(D)** DLR provides higher spatial resolution and reduces blooming artifacts compared with FBP and HIR at all dose levels without degrading the smooth margin, yielding a well-balanced image appearance. The reconstruction time for the FBP, HIR, MBIR, and DLR images was 10, 13, 191, and 30 seconds, respectively.

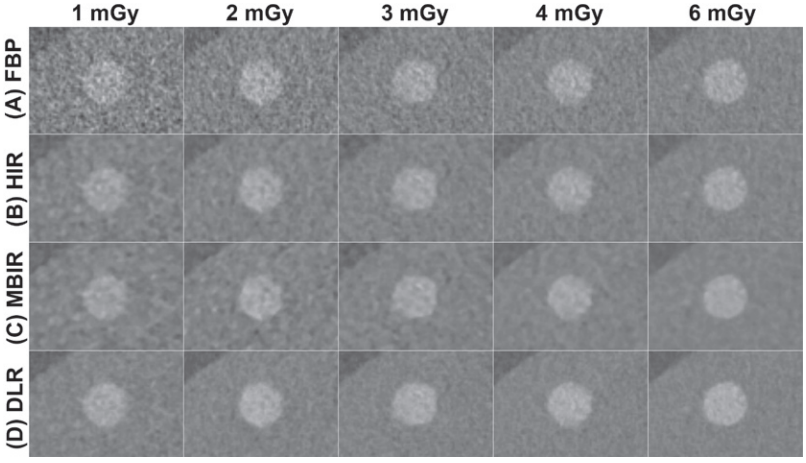

Figure 9. Axial CT images obtained with FBP **(A)**, HIR **(B)**, MBIR **(C)**, and DLR **(D)** and centered on the acrylic insert of a Catphan CTP682 module (The Phantom Laboratory) as a function of the dose level. The reconstruction time for the FBP, HIR, MBIR, and DLR images was 10, 13, 191, and 30 seconds, respectively.

at lower dose levels (Fig 8b), probably because the iterative filtration would strongly work to compensate for increased noise and degrade the spatial resolution (45,49).

MBIR generally improves high-contrast spatial resolution (17,49–52), but jagged edge artifact and steplike appearance may be noted at lower dose levels (Fig 8c) (53–55). These imaging features can negatively affect the subjective acceptability and image interpretation in some clinical conditions, particularly when radiologists and physicians are unfamiliar with the unique image appearance of MBIR (54,55).

In phantom images, DLR yields superior high-contrast spatial resolution to those of FBP and HIR at clinically relevant dose ranges while preserving a smooth margin, providing an overall acceptable image appearance (45,47,48,56) (Fig 8d).

Depiction of Low-Contrast Object

In FBP images, delineation of low-contrast objects can be degraded at lower dose settings because of the considerably amplified image noise. IR techniques partially overcome the limitation of FBP, although maintaining adequate low-contrast object detectability is still challenging (21,22). As shown in Figure 9, delineation of low-contrast objects can be blurred with both HIR and MBIR at lower doses owing to the prominent low-spatial-frequency noise component. In contrast, the low-contrast object can be clearly and sharply delineated in DLR images even at the lowest dose range owing to the finer noise property with preserved low-contrast resolution (45,47,48,56).

Dose-Reduction Potential

Considering the characteristics of the image mentioned earlier, application of DLR may allow greater dose reduction compared with those of the FBP and IR techniques. Preliminary phantom and clinical investigations have shown that DLR yields 30%–80% dose reduction compared with current standard-of-care HIR algorithms without loss of diagnostic image quality (47,48,57,58). Concordant with these reports, our phantom images imply that DLR enables at least 50% dose reduction compared with that of HIR, without sacrificing clear depiction of clinically relevant high- and low-contrast objects

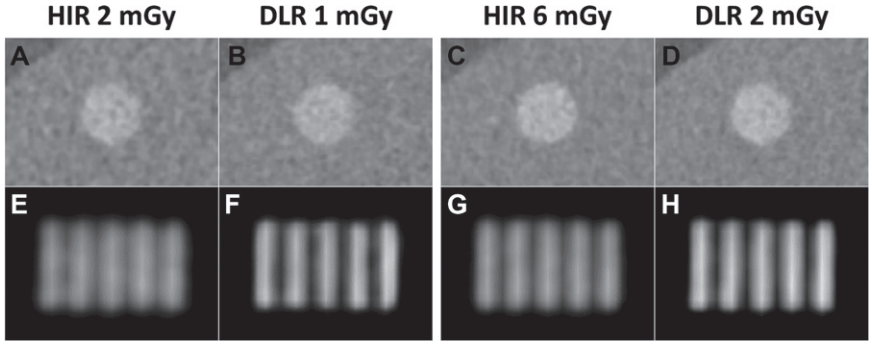

Figure 10. CT images of low-contrast **(A–D)** and high-contrast **(E–H)** objects reconstructed with higher-dose HIR and lower-dose DLR. Compared with the HIR images obtained at 2 mGy **(A, E)** and 6 mGy **(C, G)**, the DLR images obtained at 1 mGy **(B, F)** and 2 mGy **(D, H)** show equivalent or even better object depiction.

Strengths and Limitations of Different Image-Reconstruction Techniques

Parameter	FBP	HIR	MBIR	DLR
Reconstruction speed	Very fast	Very fast	Slow	Fast
Noise reduction	None	Moderate	Strong	Strong
Noise texture	Natural and well-familiarized texture for radiologists	Relatively natural but degraded at lower dose and stronger levels	Pixelated, blotchy, and unnatural texture, particularly at low dose	Natural and fine texture even at low dose settings
Spatial resolution	Moderate	Moderate but degraded at low dose	High	High
Dose-reduction capability for high-contrast object tasks*	None	Moderate	High	High
Dose-reduction capability for low-contrast object tasks†	None	Moderate	Moderate	High

*Examples include lung CT, bone CT, CT angiography, and head CT for hydrocephalus evaluation.
†Examples include brain CT and abdominal CT for parenchymal organ assessment.

(Fig 10). The Table summarizes the reconstruction speed, image characteristics, and possible dose-reduction capabilities of each image-reconstruction technique.

Current Possible Issues of DLR

Despite its promising dose-reduction potential, some possible concerns about the DLR technique may remain. For instance, some subtle lesions that are not sufficiently represented in training and testing sets could not be clearly depicted in DLR images, particularly at considerably reduced dose settings, as with other reconstruction techniques. In addition, it is currently unclear whether radiologists can correctly recognize possible false-negative or false-positive findings in seemingly high-quality DLR images that are acquired with inappropriately reduced radiation doses.

Given that the effect of DLR on image quality and diagnostic performance is still in the early stages of research, future human observer performance investigations—using phantoms containing various artificial lesions or clinical images acquired at various dose settings—may further rigorously determine the extent to which dose reduction can be achieved without deteriorating diagnostic performance for each clinical condition.

Application of DLR for Low-Dose Pediatric CT

In this section, we present representative clinical cases to demonstrate the feasibility of DLR for reduced-dose pediatric CT for a variety of diagnostic indications. All DLR images were reconstructed using AiCE algorithms optimized for each diagnostic task.

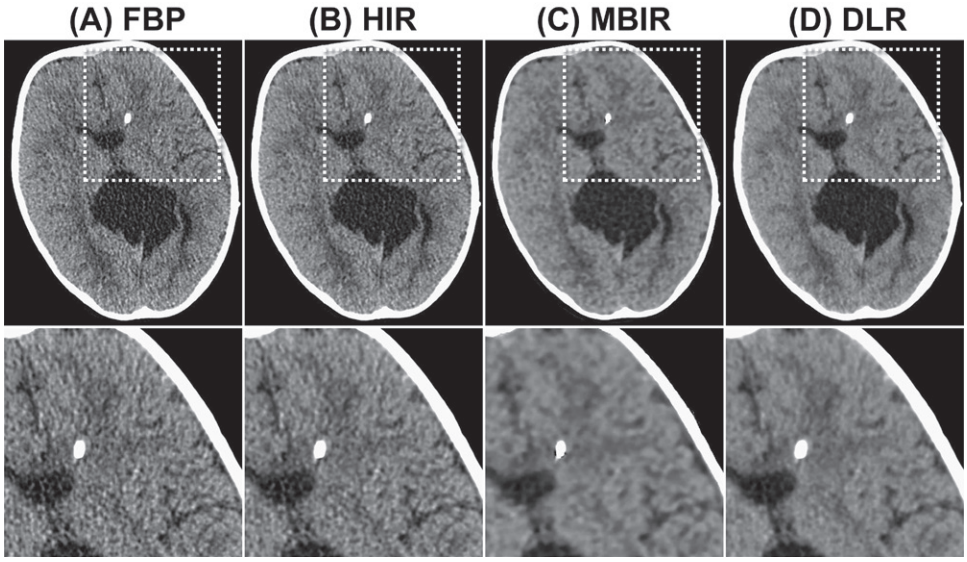

Figure 11. Axial noncontrast head CT images in a 3-year-old boy with a cerebrospinal fluid shunt. Images were acquired at a $CTDI_{vol}$ of 15 mGy and reconstructed with FBP **(A)**, HIR **(B)**, MBIR **(C)**, and DLR **(D)**. The section thickness for all images was 1 mm. The DLR image provides better gray-white matter contrast and lower noise magnitude than the FBP and HIR images and preserves a more natural and sharp appearance than the MBIR image. The reconstruction time for the FBP, HIR, MBIR, and DLR images was 11, 12, 144, and 25 seconds, respectively.

Figure 12. Sagittal noncontrast CT images in a 1-day-old boy with subdural hemorrhage. Images were acquired at a $CTDI_{vol}$ of 14 mGy and reconstructed with FBP **(A)**, HIR **(B)**, and DLR **(C)**. The section thickness for all images was 1 mm. In the DLR image, the extent of hemorrhage is better delineated than in the FBP and HIR images owing to a considerable reduction in image noise and improved low-contrast resolution. The reconstruction time for the FBP, HIR, and DLR images was 11, 12, and 26 seconds, respectively.

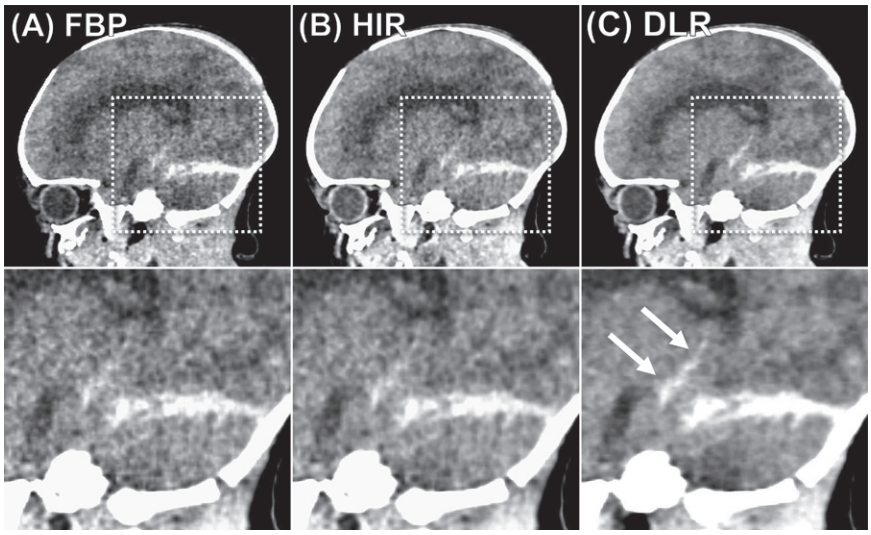

Head CT

Head CT is reportedly the most frequent CT examination performed in pediatric patients (2). Therefore, dose optimization would substantially reduce the overall radiation exposure. In this diagnostic task, acquisition of low-noise images with sufficient low-contrast spatial resolution is required to clearly delineate subtle contrast differences, such as gray-white matter contrast.

Although IR may allow a certain degree of dose reduction without deteriorating image quality (59–62), application of a strong noise-reduction mode at considerably reduced dose settings may compromise the subjective acceptability and diagnostic performance owing to degraded noise texture and low-contrast spatial resolution (59,60). DLR reduces image noise drastically and improves low-contrast resolution while preserving preferable noise texture, providing greater dose-reduction opportunity for pediatric head CT than IR techniques (63,64) (Figs 11, 12).

Temporal Bone CT

Temporal bone CT is an essential diagnostic tool for identifying anatomic variants and abnormalities in the middle ear and inner ear, where acquisition of high-spatial-resolution images is imperative to depict complex-shaped subtle bone structures. Despite the reported dose-reduction capability of IR (65,66), there have been con-

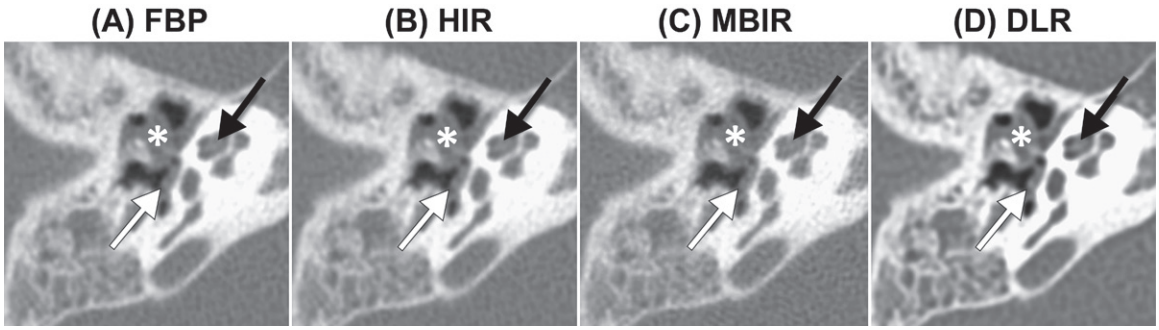

Figure 13. Axial temporal bone CT images in a 7-year-old girl with a right cholesteatoma. Images were acquired at a $CTDI_{vol}$ of 10 mGy and reconstructed with FBP **(A)**, HIR **(B)**, MBIR **(C)**, and DLR **(D)** using high-spatial inner-ear modes. All bone structures—including the stapes (white arrow) and spiral osseous lamina (black arrow)—as well as the cholesteatoma (*) are more clearly and sharply delineated in the DLR image. The reconstruction time for the FBP, HIR, MBIR, and DLR images was 15, 16, 112, and 24 seconds, respectively.

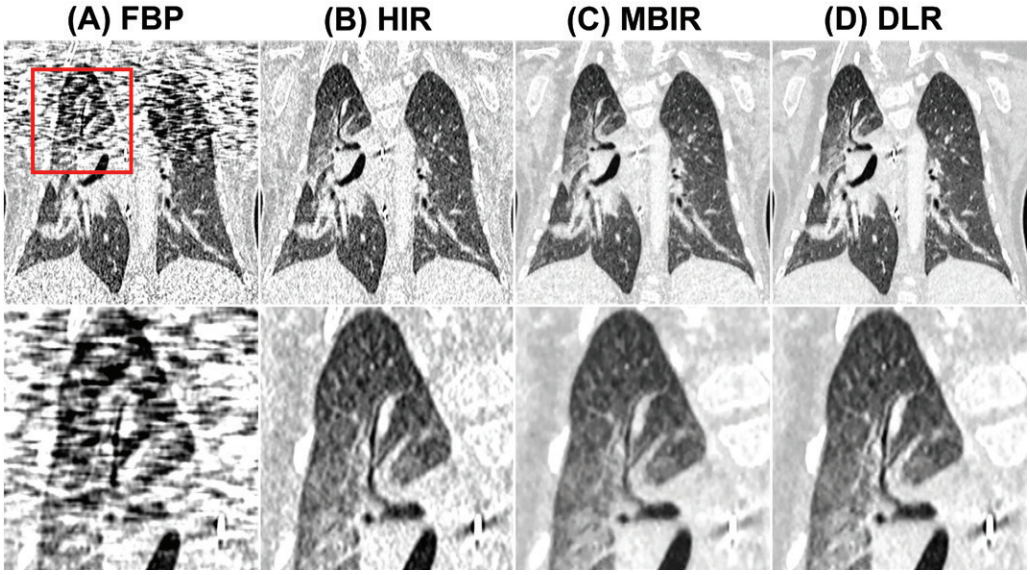

Figure 14. Coronal lung CT images in an 8-month-old boy (body weight, 8 kg) with pneumonia. Images were acquired at a $CTDI_{vol}$ of 0.6 mGy in the arms-down position and reconstructed with FBP **(A)**, HIR **(B)**, MBIR **(C)**, and DLR **(D)** with lung modes. The FBP image shows severe streak artifact at the shoulder level (red square), resulting in undiagnostic image quality. Despite substantial artifact reduction, the HIR and MBIR images show noisy and blurred image appearance, respectively. In the DLR image, fine structures and anatomic interfaces are sharply delineated without being obscured by noise and artifact. The reconstruction time for the FBP, HIR, MBIR, and DLR images was 10, 11, 130, and 40 seconds, respectively.

cerns that delineation of the finest structures—such as the spiral osseous lamina and stapes—can be compromised by using a strong level of HIR or MBIR (67,68). In our initial clinical experience, DLR can enhance subtle structures' depiction without increasing noise, thereby possibly serving as a better alternative to IR for low-dose temporal bone CT (Fig 13).

Lung CT

The chest is a high-contrast and low-attenuation anatomic area owing to air-filled lung parenchyma, which allows aggressive radiation dose reduction to obtain diagnostically adequate information. Compared with FBP and HIR algorithms, MBIR yields greater noise and artifact reduction without affecting lung nodule detectability in ultralow-dose lung CT (69,70).

Nevertheless, alteration of noise texture can cause blurring of subtle anatomic structures, decreased visibility of important abnormalities—such as interlobular septal thickening—and steplike appearance at the tissue interface (55,71,72). With DLR, the noise and artifact may be reduced to a level almost comparable to that of MBIR images, whereas edge sharpness, depiction of subtle anatomic structures, and natural image appearance are well preserved (Figs 14, 15).

Spine CT

Although plain radiography is the first-line imaging modality for evaluation of spinal abnormalities,

Figure 15. Axial lung CT images in an 8-year-old boy (body weight, 25 kg) with pulmonary hemosiderosis. Images were acquired at a $CTDI_{vol}$ of 1.8 mGy and reconstructed with FBP **(A)**, MBIR **(B)**, and DLR **(C)** with lung modes. Low noise, high spatial resolution, and natural noise texture are all achieved in the DLR image. The reconstruction time for the FBP, MBIR, and DLR images was 11, 152, and 48 seconds, respectively.

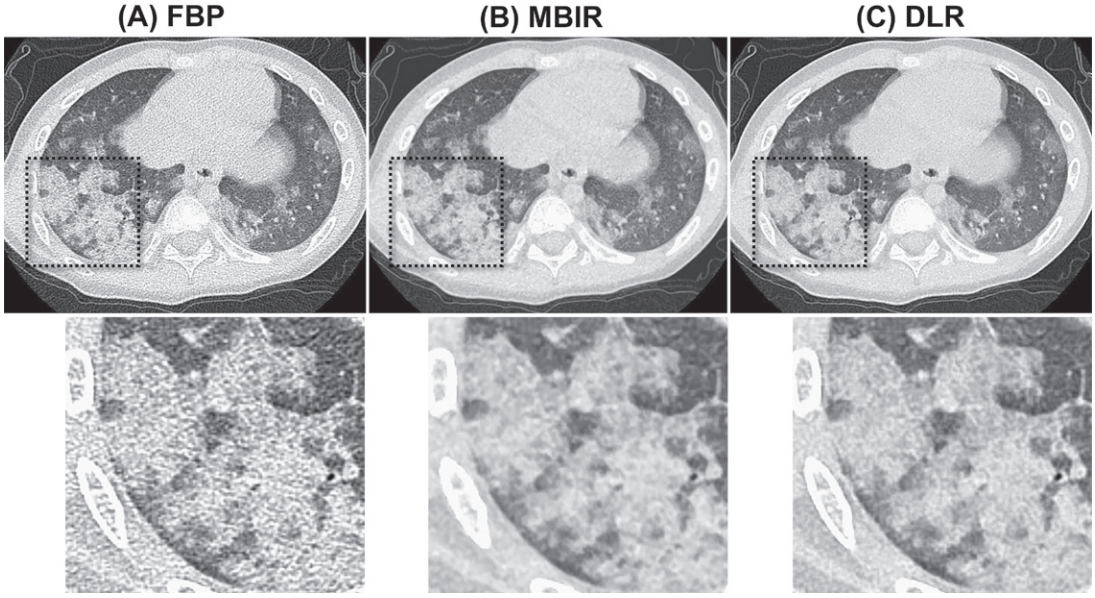

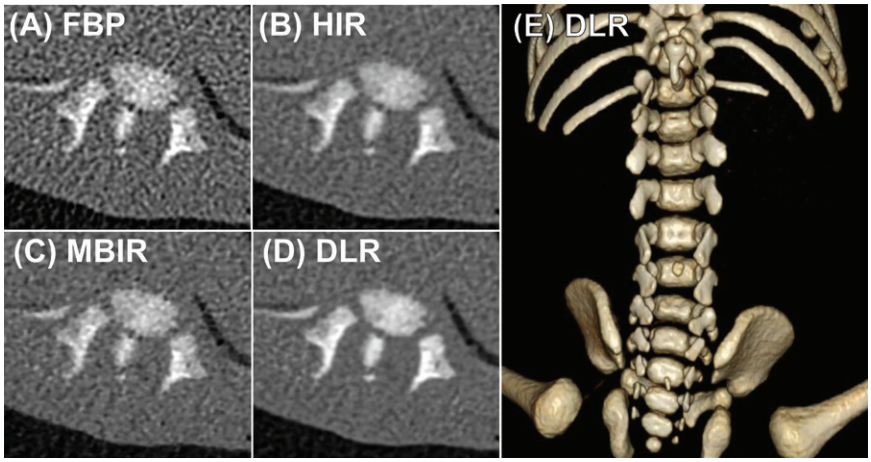

Figure 16. Axial spine CT images in a 1-day-old newborn girl (body weight, 3.4 kg) with diastematomyelia. Images were acquired at a $CTDI_{vol}$ of 0.3 mGy and reconstructed with FBP **(A)**, HIR **(B)**, MBIR **(C)**, and DLR **(D)** with bone modes. Image granularity and the resulting bone margin irregularity are minimized in the DLR image, yielding a high-quality volume-rendered image **(E)**. The reconstruction time for the FBP, HIR, MBIR, and DLR images was 8, 8, 89, and 23 seconds, respectively.

such as traumatic injury, spina bifida, and scoliosis, spine CT provides more detailed anatomic information, yielding accurate diagnosis and optimal surgical planning. As in lung CT, the radiation dose can be substantially lowered without loss of diagnostic values because the high intrinsic contrast between the bone and surrounding soft tissue provides tolerability for increased noise (73). Compared with FBP and IR techniques, DLR may provide cross-sectional and volume-rendered images with less graininess, smoother bone surface, and better delineation of small bone structures at considerably reduced-dose spine CT (Fig 16).

CT Angiography

CT angiography plays a pivotal role in accurate diagnosis and optimal management of various vascular abnormalities, including congenital malformations and traumatic injuries. Delineation of tiny vessels can be degraded in reduced-dose FBP and HIR images because of increased noise and limited spatial resolution. MBIR usually yields the best depiction of small vessels owing to improved high-contrast spatial resolution (42,45), but blotchy noise texture and jagged vessel appearance may be noticeable in low-dose settings. DLR would play a complementary role

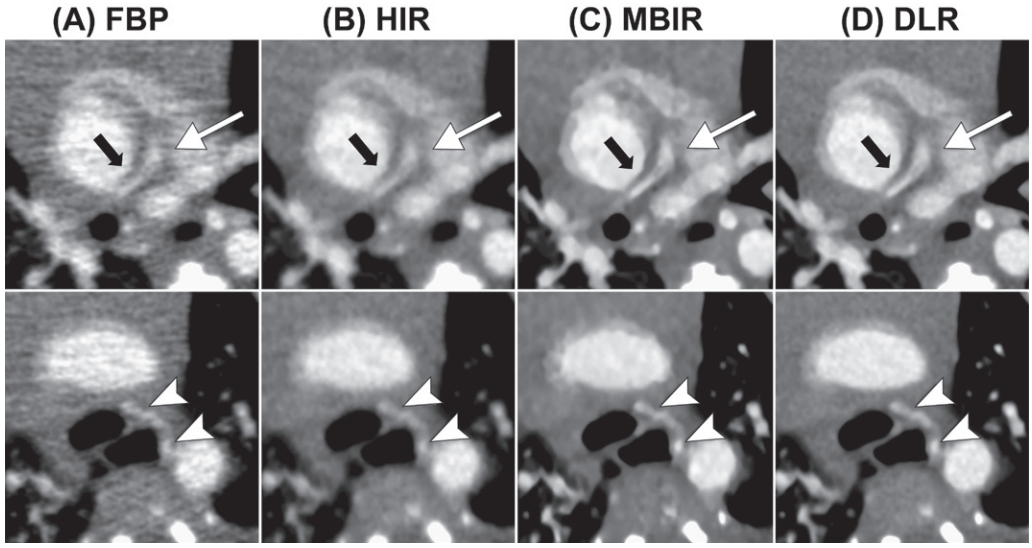

Figure 17. Axial CT angiograms in an 8-day-old girl (body weight, 3 kg) with pulmonary atresia and major aortopulmonary collateral artery (MAPCA). Images were acquired at a $CTDI_{vol}$ of 0.5 mGy and reconstructed with FBP **(A)**, HIR **(B)**, MBIR **(C)**, and DLR **(D)**. With DLR, the right ventricular outflow tract obstruction (white arrow), small pulmonary artery (black arrow), and MAPCA (white arrowheads) are clearly depicted while ensuring a sharp and smooth structure margin. The reconstruction time for the FBP, HIR, MBIR, and DLR images was 13, 14, 148, and 29 seconds, respectively.

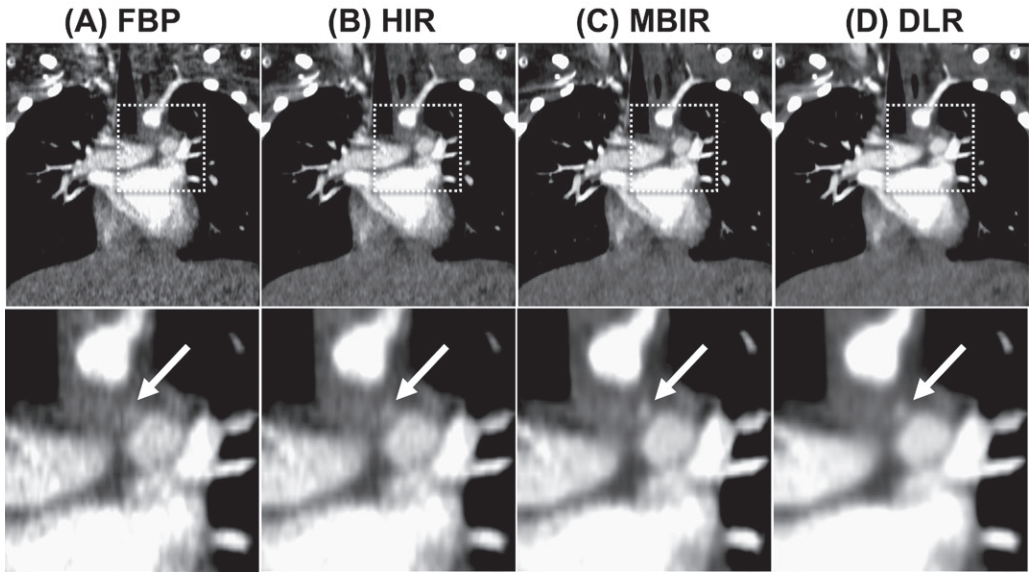

Figure 18. Coronal CT angiograms in a 1-year-old girl (body weight, 9 kg) with patent ductus arteriosus (PDA). Images were acquired at a $CTDI_{vol}$ of 0.6 mGy and reconstructed with FBP **(A)**, HIR **(B)**, MBIR **(C)**, and DLR **(D)**. The small PDA (arrow), obscured in the FBP and HIR images, is clearly delineated in the MBIR and DLR images because of superior spatial resolution. The reconstruction time for the FBP, HIR, MBIR, and DLR images was 17, 18, 160, and 26 seconds, respectively.

to MBIR, because it improves delineation of small vessels in comparison with FBP and HIR without compromising the natural texture and edge smoothness at short reconstruction times (Figs 17, 18) (42,45).

Abdominal CT

Abdominal CT is the second most frequent and largest source of effective dose in pediatric CT (2); thus, implementation of dose-optimization strategies is crucial. IR techniques facilitate drastic dose reduction in abdominal CT for high-contrast tasks, such as detecting urinary stones and diagnosing appendicitis (74). Nevertheless, its dose-reduction capability may still be limited for parenchymal organ evaluation involving detection and characterization of low-contrast lesions (21,22). As has been suggested in prior phantom and clinical studies (42,45,47,57,58,75), DLR may currently be the best reconstruction method to

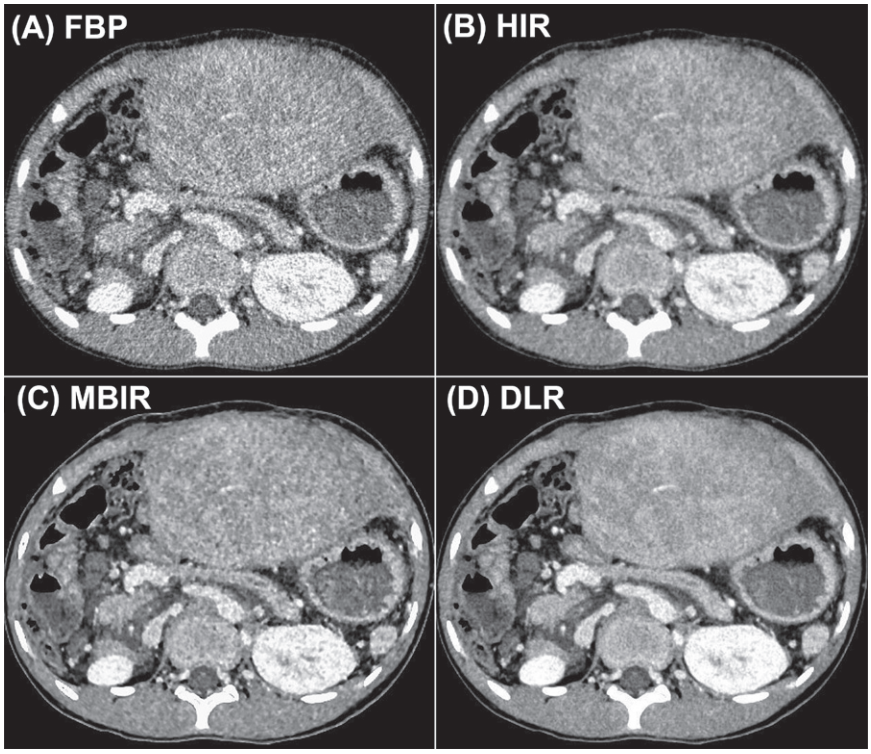

Figure 19. Axial contrast-enhanced abdominal CT images in a 13-year-old boy (body weight, 40 kg) after liver transplantation for fulminant hepatitis of unknown cause. Images were acquired with a $CTDI_{vol}$ of 3.2 mGy and reconstructed with FBP **(A)**, HIR **(B)**, MBIR **(C)**, and DLR **(D)**. Heterogeneous liver parenchymal texture caused by fibrosis is confidently evaluated in the DLR image owing to considerably reduced image noise and preserved fine noise texture via reduced low-frequency noise components. The reconstruction time for the FBP, HIR, MBIR, and DLR images was 28, 36, 210, and 43 seconds, respectively.

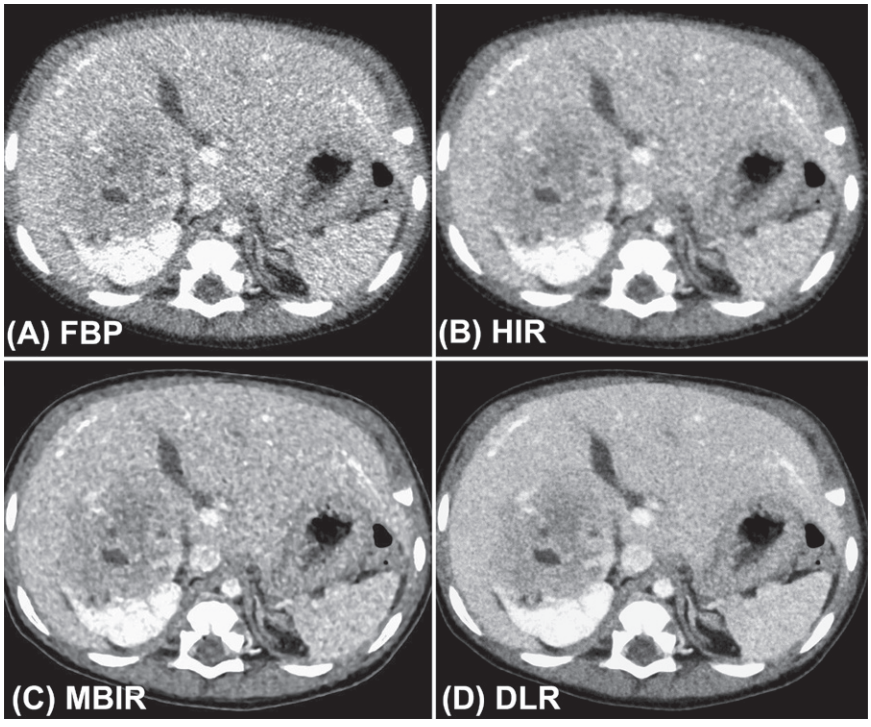

Figure 20. Axial contrast-enhanced abdominal CT images in an 8-month-old boy (body weight, 8.6 kg) with right Wilms tumor. Images were acquired with a $CTDI_{vol}$ of 0.8 mGy and reconstructed with FBP **(A)**, HIR **(B)**, MBIR **(C)**, and DLR **(D)**. Pixelated image appearance and coarse noise texture in the HIR and MBIR images are almost completely removed in the DLR image without loss of low-contrast resolution. The reconstruction time for the FBP, HIR, MBIR, and DLR images was 24, 24, 366, and 54 seconds, respectively.

achieve low-dose high-quality pediatric abdominal CT owing to its capability for drastic noise reduction, improved noise texture, and clear delineation of low-contrast objects (Figs 19–21).

Conclusion

Implementation of dose-optimization techniques in daily clinical practice is imperative to mitigate the possible adverse effects of ionizing radiation exposure from pediatric CT. With the advancement of artificial intelligence (AI) technologies, novel DLR algorithms that incorporate CNNs into the image reconstruction process have been introduced and are now available clinically. DLR is a promising tool for obtaining CT images with substantially reduced noise, sufficient spatial

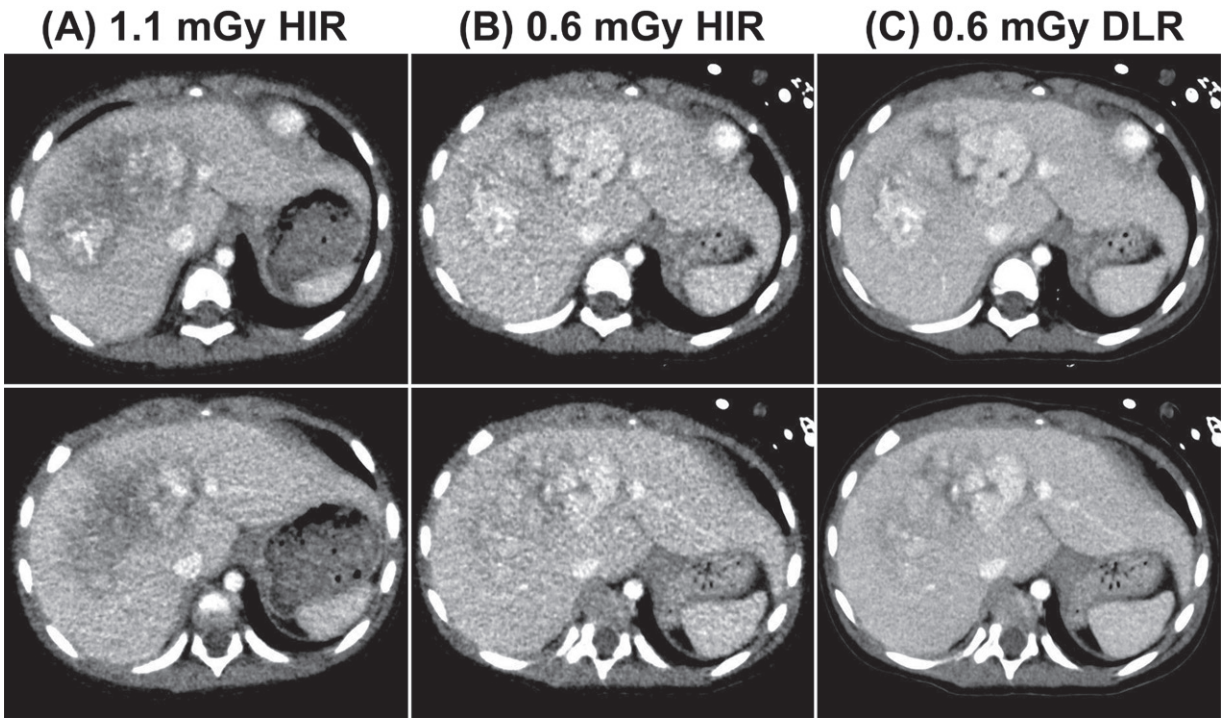

Figure 21. Axial contrast-enhanced abdominal CT images in a 1-year-old boy with hepatoblastoma who underwent two CT examinations at a 6-month interval. **(A)** Axial CT images acquired with standard-of-care dose setting ($CTDI_{vol}$, 1.1 mGy) and reconstructed with HIR. **(B, C)** Axial CT images acquired with reduced dose setting ($CTDI_{vol}$, 0.6 mGy) and reconstructed with HIR **(B)** and DLR **(C)**. DLR considerably improved lesion conspicuity compared with HIR while preserving lower image noise and preferable noise texture than the standard-dose HIR image even at almost half dose. The reconstruction time for the reduced-dose HIR and DLR images was 11 and 28 seconds, respectively.

resolution, and preferable image texture in a short reconstruction time. As shown in this article, DLR can facilitate low-dose pediatric CT in a wide range of clinical conditions compared with traditional FBP and current standard-of-care IR techniques.

Acknowledgments.—The authors would like to acknowledge Takashi Tsutsumi, Hiroko Ueda, Shinsuke Shigematsu, Takumi Esaki, Kengo Nakato, and Masahiro Hatemura for their great support in image collection.

Disclosures of Conflicts of Interest.—**T.H.** *Activities related to the present article:* disclosed no relevant relationships. *Activities not related to the present article:* research grants from Canon Medical Systems. *Other activities:* disclosed no relevant relationships.

References

1. Brenner DJ, Hall EJ. Computed tomography: an increasing source of radiation exposure. N Engl J Med 2007;357(22):2277–2284.
2. Miglioretti DL, Johnson E, Williams A, et al. The use of computed tomography in pediatrics and the associated radiation exposure and estimated cancer risk. JAMA Pediatr 2013;167(8):700–707.
3. Pearce MS, Salotti JA, Little MP, et al. Radiation exposure from CT scans in childhood and subsequent risk of leukaemia and brain tumours: a retrospective cohort study. Lancet 2012;380(9840):499–505.
4. Berrington de Gonzalez A, Salotti JA, McHugh K, et al. Relationship between paediatric CT scans and subsequent risk of leukaemia and brain tumours: assessment of the impact of underlying conditions. Br J Cancer 2016;114(4): 388–394.
5. Lee KH, Lee S, Park JH, et al. Risk of Hematologic Malignant Neoplasms From Abdominopelvic Computed Tomographic Radiation in Patients Who Underwent Appendectomy. JAMA Surg 2021;156(4):343–351.
6. Mathews JD, Forsythe AV, Brady Z, et al. Cancer risk in 680,000 people exposed to computed tomography scans in childhood or adolescence: data linkage study of 11 million Australians. BMJ 2013;346:f2360.
7. Halm BM, Franke AA, Lai JF, et al. γ-H2AX foci are increased in lymphocytes in vivo in young children 1 h after very low-dose X-irradiation: a pilot study. Pediatr Radiol 2014;44(10):1310–1317.
8. Vandevoorde C, Franck C, Bacher K, et al. γ-H2AX foci as in vivo effect biomarker in children emphasize the importance to minimize x-ray doses in paediatric CT imaging. Eur Radiol 2015;25(3):800–811.
9. Kalra MK, Sodickson AD, Mayo-Smith WWCT. CT Radiation: Key Concepts for Gentle and Wise Use. RadioGraphics 2015;35(6):1706–1721.
10. Herzog C, Mulvihill DM, Nguyen SA, et al. Pediatric cardiovascular CT angiography: radiation dose reduction using automatic anatomic tube current modulation. AJR Am J Roentgenol 2008;190(5):1232–1240.
11. Bodelle B, Fischbach C, Booz C, et al. Free-breathing high-pitch 80kVp dual-source computed tomography of the pediatric chest: image quality, presence of motion artifacts and radiation dose. Eur J Radiol 2017;89:208–214.
12. Nagayama Y, Oda S, Nakaura T, et al. Radiation Dose Reduction at Pediatric CT: Use of Low Tube Voltage and Iterative Reconstruction. RadioGraphics 2018;38(5):1421–1440.
13. Weis M, Henzler T, Nance JW Jr, et al. Radiation Dose Comparison Between 70 kVp and 100 kVp With Spectral Beam Shaping for Non-Contrast-Enhanced Pediatric Chest Computed Tomography: A Prospective Randomized Controlled Study. Invest Radiol 2017;52(3):155–162.
14. von Falck C, Galanski M, Shin HO. Informatics in radiology: sliding-thin-slab averaging for improved depiction

of low-contrast lesions with radiation dose savings at thin-section CT. RadioGraphics 2010;30(2):317–326.
15. Mahesh M. Search for isotropic resolution in CT from conventional through multiple-row detector. RadioGraphics 2002;22(4):949–962.
16. Geyer LL, Schoepf UJ, Meinel FG, et al. State of the Art: Iterative CT Reconstruction Techniques. Radiology 2015;276(2):339–357.
17. Stiller W. Basics of iterative reconstruction methods in computed tomography: a vendor-independent overview. Eur J Radiol 2018;109:147–154.
18. Willemink MJ, Noël PB. The evolution of image reconstruction for CT: from filtered back projection to artificial intelligence. Eur Radiol 2019;29(5):2185–2195.
19. Higaki T, Nakamura Y, Fukumoto W, Honda Y, Tatsugami F, Awai K. Clinical application of radiation dose reduction at abdominal CT. Eur J Radiol 2019;111:68–75.
20. Ehman EC, Yu L, Manduca A, et al. Methods for clinical evaluation of noise reduction techniques in abdominopelvic CT. RadioGraphics 2014;34(4):849–862.
21. McCollough CH, Yu L, Kofler JM, et al. Degradation of CT Low-Contrast Spatial Resolution Due to the Use of Iterative Reconstruction and Reduced Dose Levels. Radiology 2015;276(2):499–506.
22. Mileto A, Guimaraes LS, McCollough CH, Fletcher JG, Yu L. State of the Art in Abdominal CT: The Limits of Iterative Reconstruction Algorithms. Radiology 2019;293(3):491–503.
23. Samei E, Bakalyar D, Boedeker KL, et al. Performance evaluation of computed tomography systems: summary of AAPM Task Group 233. Med Phys 2019;46(11):e735–e756.
24. Zhou Y. Dose and blending fraction quantification for adaptive statistical iterative reconstruction based on low-contrast detectability in abdomen CT. J Appl Clin Med Phys 2020;21(2):128–135.
25. Mileto A, Zamora DA, Alessio AM, et al. CT Detectability of Small Low-Contrast Hypoattenuating Focal Lesions: Iterative Reconstructions versus Filtered Back Projection. Radiology 2018;289(2):443–454.
26. Jensen CT, Wagner-Bartak NA, Vu LN, et al. Detection of Colorectal Hepatic Metastases Is Superior at Standard Radiation Dose CT versus Reduced Dose CT. Radiology 2019;290(2):400–409.
27. LeCun Y, Bengio Y, Hinton G. Deep learning. Nature 2015;521(7553):436–444.
28. Chartrand G, Cheng PM, Vorontsov E, et al. Deep learning: A Primer for Radiologists. RadioGraphics 2017;37(7):2113–2131.
29. Choy G, Khalilzadeh O, Michalski M, et al. Current Applications and Future Impact of Machine Learning in Radiology. Radiology 2018;288(2):318–328.
30. Yamashita R, Nishio M, Do RKG, Togashi K. Convolutional neural networks: an overview and application in radiology. Insights Imaging 2018;9(4):611–629.
31. Yasaka K, Akai H, Kunimatsu A, Kiryu S, Abe O. Deep learning with convolutional neural network in radiology. Jpn J Radiol 2018;36(4):257–272.
32. Soffer S, Ben-Cohen A, Shimon O, Amitai MM, Greenspan H, Klang E. Convolutional Neural Networks for Radiologic Images: A Radiologist's Guide. Radiology 2019;290(3):590–606.
33. He K, Zhang X, Ren S, Sun J. Deep Residual Learning for Image Recognition. In: 2016 IEEE Conference on Computer Vision and Pattern Recognition (CVPR), Las Vegas, Nev, June 27–30, 2016. Piscataway, NJ: IEEE, 2016; 770–778.
34. Ioffe S, Szegedy C. Batch Normalization: Accelerating Deep Network Training by Reducing Internal Covariate Shift. In: Bach F, Blei D, eds. Proceedings of the 32nd International Conference on Machine Learning: Proceedings of Machine Learning Research (PMLR), Lille, France, July 6–11, 2015. J Mach Learn Res: JMLR 2015;37:448–456.
35. Ueda D, Yamamoto A, Nishimori M, et al. Deep Learning for MR Angiography: Automated Detection of Cerebral Aneurysms. Radiology 2019;290(1):187–194.
36. Yasaka K, Akai H, Kunimatsu A, Abe O, Kiryu S. Liver Fibrosis: Deep Convolutional Neural Network for Staging by Using Gadoxetic Acid–enhanced Hepatobiliary Phase MR Images. Radiology 2018;287(1):146–155.
37. Norman B, Pedoia V, Majumdar S. Use of 2D U-Net Convolutional Neural Networks for Automated Cartilage and Meniscus Segmentation of Knee MR Imaging Data to Determine Relaxometry and Morphometry. Radiology 2018;288(1):177–185.
38. Lei Y, Harms J, Wang T, et al. MRI-only based synthetic CT generation using dense cycle consistent generative adversarial networks. Med Phys 2019;46(8):3565–3581.
39. Zhang K, Zuo W, Chen Y, Meng D, Zhang L. Beyond a Gaussian Denoiser: Residual Learning of Deep CNN for Image Denoising. IEEE Trans Image Process 2017;26(7):3142–3155.
40. Chen H, Zhang Y, Kalra MK, et al. Low-Dose CT With a Residual Encoder-Decoder Convolutional Neural Network. IEEE Trans Med Imaging 2017;36(12):2524–2535.
41. Nakamura Y, Higaki T, Tatsugami F, et al. Deep Learning-based CT Image Reconstruction: Initial Evaluation Targeting Hypovascular Hepatic Metastases. Radiol Artif Intell 2019;1(6):e180011.
42. Akagi M, Nakamura Y, Higaki T, et al. Deep learning reconstruction improves image quality of abdominal ultra-high-resolution CT. Eur Radiol 2019;29(11):6163–6171. [Published correction appears in Eur Radiol 2019;29(8):4526–4527.]
43. Tatsugami F, Higaki T, Nakamura Y, et al. Deep learning-based image restoration algorithm for coronary CT angiography. Eur Radiol 2019;29(10):5322–5329.
44. Hsieh J, Liu E, Nett B, Tang J, Thibault JB, Sahney S. A new era of image reconstruction: TrueFidelity—technical white paper on deep learning image reconstruction. Chicago, Illinois: GE Healthcare, 2019.
45. Higaki T, Nakamura Y, Zhou J, et al. Deep Learning Reconstruction at CT: Phantom Study of the Image Characteristics. Acad Radiol 2020;27(1):82–87.
46. Samei E, Richard S. Assessment of the dose reduction potential of a model-based iterative reconstruction algorithm using a task-based performance metrology. Med Phys 2015;42(1):314–323.
47. Greffier J, Hamard A, Pereira F, et al. Image quality and dose reduction opportunity of deep learning image reconstruction algorithm for CT: a phantom study. Eur Radiol 2020;30(7):3951–3959.
48. Kawashima H, Ichikawa K, Takata T, et al. Performance of clinically available deep learning image reconstruction in computed tomography: a phantom study. J Med Imaging (Bellingham) 2020;7(6):063503.
49. Greffier J, Frandon J, Larbi A, Beregi JP, Pereira F. CT iterative reconstruction algorithms: a task-based image quality assessment. Eur Radiol 2020;30(1):487–500.
50. Tatsugami F, Higaki T, Sakane H, et al. Coronary Artery Stent Evaluation with Model-based Iterative Reconstruction at Coronary CT Angiography. Acad Radiol 2017;24(8):975–981.
51. Higaki T, Tatsugami F, Fujioka C, et al. Visualization of simulated small vessels on computed tomography using a model-based iterative reconstruction technique. Data Brief 2017;13:437–443.
52. Yokomachi K, Tatsugami F, Higaki T, et al. Neointimal formation after carotid artery stenting: phantom and clinical evaluation of model-based iterative reconstruction (MBIR). Eur Radiol 2019;29(1):161–167.
53. Li G, Liu X, Dodge CT, Jensen CT, Rong XJ. A noise power spectrum study of a new model-based iterative reconstruction system: Veo 3.0. J Appl Clin Med Phys 2016;17(5):428–439.
54. Aurumskjöld ML, Söderberg M, Stålhammar F, von Steyern KV, Tingberg A, Ydström K. Evaluation of an iterative model-based reconstruction of pediatric abdominal CT with regard to image quality and radiation dose. Acta Radiol 2018;59(6):740–747.
55. Hata A, Yanagawa M, Honda O, Gyobu T, Ueda K, Tomiyama N. Submillisievert CT using model-based iterative reconstruction with lung-specific setting: an initial phantom study. Eur Radiol 2016;26(12):4457–4464.
56. Racine D, Becce F, Viry A, et al. Task-based characterization of a deep learning image reconstruction and comparison with filtered back-projection and a partial model-based iterative

reconstruction in abdominal CT: a phantom study. Phys Med 2020;76:28–37.
57. Nakamura Y, Narita K, Higaki T, Akagi M, Honda Y, Awai K. Diagnostic value of deep learning reconstruction for radiation dose reduction at abdominal ultra-high-resolution CT. Eur Radiol 2021;31(7):4700–4709.
58. Singh R, Digumarthy SR, Muse VV, et al. Image Quality and Lesion Detection on Deep Learning Reconstruction and Iterative Reconstruction of Submillisievert Chest and Abdominal CT. AJR Am J Roentgenol 2020;214(3):566–573.
59. Mirro AE, Brady SL, Kaufman RA. Full Dose-Reduction Potential of Statistical Iterative Reconstruction for Head CT Protocols in a Predominantly Pediatric Population. AJNR Am J Neuroradiol 2016;37(7):1199–1205.
60. Southard RN, Bardo DME, Temkit MH, Thorkelson MA, Augustyn RA, Martinot CA. Comparison of Iterative Model Reconstruction versus Filtered Back-Projection in Pediatric Emergency Head CT: Dose, Image Quality, and Image-Reconstruction Times. AJNR Am J Neuroradiol 2019;40(5):866–871.
61. Nagayama Y, Nakaura T, Tsuji A, et al. Radiation dose reduction using 100-kVp and a sinogram-affirmed iterative reconstruction algorithm in adolescent head CT: impact on grey-white matter contrast and image noise. Eur Radiol 2017;27(7):2717–2725.
62. Kim HG, Lee HJ, Lee SK, Kim HJ, Kim MJ. Head CT: image quality improvement with ASIR-V using a reduced radiation dose protocol for children. Eur Radiol 2017;27(9):3609–3617.
63. Kim I, Kang H, Yoon HJ, Chung BM, Shin NY. Deep learning-based image reconstruction for brain CT: improved image quality compared with adaptive statistical iterative reconstruction-Veo (ASIR-V). Neuroradiology 2021;63(6):905–912.
64. Oostveen LJ, Meijer FJA, de Lange F, et al. Deep learning-based reconstruction may improve non-contrast cerebral CT imaging compared to other current reconstruction algorithms. Eur Radiol 2021. doi: 10.1007/s00330-020-07668-x. Published online March 10, 2021. Accessed March 24, 2021.
65. Niu YT, Mehta D, Zhang ZR, et al. Radiation dose reduction in temporal bone CT with iterative reconstruction technique. AJNR Am J Neuroradiol 2012;33(6):1020–1026.
66. Leng S, Diehn FE, Lane JI, et al. Temporal Bone CT: Improved Image Quality and Potential for Decreased Radiation Dose Using an Ultra-High-Resolution Scan Mode with an Iterative Reconstruction Algorithm. AJNR Am J Neuroradiol 2015;36(9):1599–1603.
67. Kurokawa R, Maeda E, Mori H, et al. Evaluation of the depiction ability of the microanatomy of the temporal bone in quarter-detector CT: model-based iterative reconstruction vs hybrid iterative reconstruction. Medicine (Baltimore) 2019;98(24):e15991.
68. Hempel JM, Niklas Bongers M, Braun K, Ernemann U, Bier G. Noise reduction and image quality in ultra-high resolution computed tomography of the temporal bone using advanced modeled iterative reconstruction. Acta Radiol 2019;60(9):1135–1143.
69. Katsura M, Matsuda I, Akahane M, et al. Model-based iterative reconstruction technique for radiation dose reduction in chest CT: comparison with the adaptive statistical iterative reconstruction technique. Eur Radiol 2012;22(8):1613–1623.
70. Yamada Y, Jinzaki M, Tanami Y, et al. Model-based iterative reconstruction technique for ultralow-dose computed tomography of the lung: a pilot study. Invest Radiol 2012;47(8):482–489.
71. Padole A, Singh S, Ackman JB, et al. Submillisievert chest CT with filtered back projection and iterative reconstruction techniques. AJR Am J Roentgenol 2014;203(4):772–781.
72. Yanagawa M, Gyobu T, Leung AN, et al. Ultra-low-dose CT of the lung: effect of iterative reconstruction techniques on image quality. Acad Radiol 2014;21(6):695–703.
73. Abul-Kasim K, Overgaard A, Maly P, Ohlin A, Gunnarsson M, Sundgren PC. Low-dose helical computed tomography (CT) in the perioperative workup of adolescent idiopathic scoliosis. Eur Radiol 2009;19(3):610–618.
74. Didier RA, Vajtai PL, Hopkins KL. Iterative reconstruction technique with reduced volume CT dose index: diagnostic accuracy in pediatric acute appendicitis. Pediatr Radiol 2015;45(2):181–187.
75. Brady SL, Trout AT, Somasundaram E, Anton CG, Li Y, Dillman JR. Improving Image Quality and Reducing Radiation Dose for Pediatric CT by Using Deep Learning Reconstruction. Radiology 2021;298(1):180–188.